Nano Research

Open Access

Research Article

Drug delivery system targeting acid sphingomyelinase reduction in vascular endothelial and neuronal cells to restore autophagy in Alzheimer's therapy

Yichong Xu[1,2], Shiyi Yu[1,2], Yan Wang[1,2], Jia Ke[1,2], Yiling Hong[1,2], Kai Wang[1,2], Guangtao Song[1,2], Zixu Wang[1,2], Si Chen[1,2], Yiru Yu[1,2], Hong Yuan[1,2], and Fuqiang Hu[1,2] ✉

[1] *College of Pharmaceutical Science, Zhejiang University, 866 Yuhangtang Road, Hangzhou 310058, China*
[2] *National Key Laboratory of Advanced Drug Delivery and Release Systems, Zhejiang University, Hangzhou 310058, China*

Cite this article: *Nano Research*, **2026**, *19*, 94908783. https://doi.org/10.26599/NR.2026.94908783

ABSTRACT: Autophagy dysfunction is intimately involved in Alzheimer's disease (AD) pathogenesis, and restoring autophagy may alleviate pathology and improve cognition. Brain microvascular endothelial cells (BMECs) represent the primary source of acid sphingomyelinase (ASM), which inhibits neuronal autophagy. Suppressing ASM in BMECs can restore autophagy and potentially treat AD. To address this target, we developed a liposomal formulation (RVG-pSL@FIN/RSV) loaded with fingolimod (FIN) and rosuvastatin (RSV), and modified with rabies virus glycoprotein (RVG) peptide to target BMECs and neurons. Upon targeting BMECs, RVG-pSL@FIN/RSV releases FIN, which serves dual functions: inhibiting ASM production in BMECs and promoting transport across the blood-brain barrier (BBB). This transport enhancement facilitates subsequent passage of RVG-pSL@FIN/RSV across the BBB to target neurons, where FIN is released to inhibit both ASM and phosphorylated tau protein (p-Tau) production. Simultaneously, RSV is released within the neurons to restore autophagy, clearing accumulated p-Tau and amyloid-beta (Aβ) proteins while inhibiting Aβ aggregation. Our dual-targeting nanodelivery system modulates BMECs and neurons, inhibiting ASM activity while enhancing trans-BBB transport. RVG-pSL@FIN/RSV reduces BMEC-derived ASM in AD mice, restores autophagy, suppresses pathogenic protein accumulation, and improves cognition. This work presents a nanodelivery system targeting BMEC-derived ASM to restore autophagy as a potential therapeutic strategy for AD.

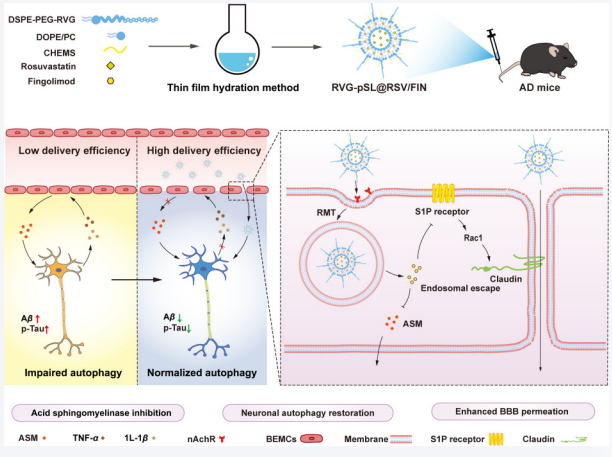

KEYWORDS: endothelial cells, acid sphingomyelinase, blood-brain barrier, autophagy, Alzheimer's disease

1 Introduction

Alzheimer's disease (AD) is a prevalent neurodegenerative disorder characterized by progressive memory loss and cognitive decline. Current clinical pharmacotherapies for AD merely alleviate symptoms without decelerating disease progression [1], imposing substantial burdens on patients and their families [2]. The primary pathological hallmarks of AD include amyloid-β (Aβ) peptide and neurofibrillary tangles (NFTs) composed of phosphorylated tau (p-Tau). Research generally acknowledges that accumulation of these pathogenic proteins, Aβ and p-Tau, constitutes the central mechanism underlying cognitive deterioration in AD patients [3]. Autophagy, an evolutionarily conserved lysosome-dependent cellular process, maintains protein homeostasis through lysosomal degradation and recycling of damaged organelles and misfolded proteins. Pathological studies of AD have revealed significantly impaired neuronal autophagy, which closely correlates with p-Tau and Aβ accumulation. Evidence suggests that restoring neuronal autophagy can facilitate clearance of pathogenic Aβ and p-Tau proteins, potentially attenuating AD progression. Strategies to enhance autophagy include inhibition of neuronal mTOR

Received: January 23, 2026; **Revised:** April 20, 2026
Accepted: April 29, 2026

✉Address correspondence to hufq@zju.edu.cn

pathways, activation of AMPK pathways, and enhancement of lysosomal acidification, among others. However, the majority of research on neuronal autophagy restoration has concentrated on neurons or microglial cells, overlooking the potential influence of brain microvascular endothelial cells (BMECs), the endothelial cells that form the blood–brain barrier (BBB), on neuronal autophagy. BMECs produce substantial quantities of acid sphingomyelinase (ASM) in AD and represent the primary source of ASM in the AD brain [4]. The secretory acid sphingomyelinase, predominantly derived from BMECs, can enter neuronal lysosomes via mannose-6-phosphate receptors (M6PRs) on the neuronal surface. This process promotes lysosomal disruption and diminishes lysosomal biogenesis by reducing the expression levels of transcription factor EB (TFEB) target genes in the nucleus, thereby exacerbating neuronal autophagic dysfunction [5]. Neuronal autophagy impairment intensifies neuroinflammation, further deteriorating the AD pathological microenvironment. Consequently, BMECs exposed to this inflammatory milieu produce additional ASM. Therefore, a therapeutic strategy that simultaneously employs autophagy enhancers directly targeting neurons while inhibiting ASM secretion from BMECs holds significant potential for more effectively restoring autophagy and achieving improved therapeutic outcomes in AD treatment.

Fingolimod (FIN), a sphingosine-1-phosphate receptor modulator approved for multiple sclerosis treatment, has been demonstrated to inhibit both ASM mRNA expression and ASM activity in various cell types including astrocytes and pancreatic cancer cells [6–8]. Furthermore, studies have established that FIN can reduce p-Tau levels [9, 10], with mechanisms involving the activation of protein phosphatase 2A (PP2A) [11]. Additionally, as a sphingosine-1-phosphate (S1P) receptor inhibitor, FIN can decrease the expression of tight junction proteins in the BBB, thereby promoting transport across the BBB and enhancing the delivery efficiency of drug delivery systems across the BBB. Statins can intervene in autophagy processes by modulating the activity or expression levels of autophagy-related proteins and genes [12]. Among statins, rosuvastatin (RSV) exhibits relatively low cytotoxicity and demonstrates excellent neuroprotective effects *in vitro* [13]. Molecular docking techniques have revealed that RSV possesses good affinity for Aβ fibrils, and its inhibitory effect on Aβ_{1-42} aggregation has been validated in rat models [14]. We hypothesize that the combined use of FIN and RSV could effectively suppress ASM secretion from BMECs while simultaneously promoting the restoration of neuronal autophagy, constituting an effective strategy to enhance therapeutic outcomes in Alzheimer's disease. However, systemic administration of FIN is associated with extensive immunosuppressive effects and cardiovascular adverse reactions. Similarly, rosuvastatin's extremely low lipophilicity results in poor central nervous system penetration, limiting its application in AD therapy [15]. The targeted design of brain drug delivery systems for intracerebral administration could effectively address the challenges associated with brain distribution of these two drugs, significantly enhancing therapeutic efficacy while reducing toxicity and adverse effects.

To address these challenges, we developed rabies virus glycoprotein (RVG) peptide-modified pH-responsive liposomes loaded with RSV and FIN (RVG-pSL@FIN/RSV) to achieve targeted delivery of FIN and RSV to BMECs and neurons, respectively. In this system, FIN downregulates ASM in BMECs, thereby facilitating transport across the BBB and promoting the brain delivery of drug delivery systems that subsequently reach the BBB. The RVG-pSL@FIN/RSV enters lysosomes in BMECs via nicotinic acetylcholine receptor-mediated endocytosis. The pH-responsive components of the liposome1,2-dioleoyl-sn-glycero-3-phosphoethanolamine (DOPE) and cholesteryl hemisuccinate (CHEMS)respond to the acidic lysosomal environment, promoting fusion between the liposome and lysosomal membrane. This process facilitates lysosomal escape, releasing FIN into the cytoplasm. FIN functions in two critical ways: it reduces ASM expression in BMECs, thereby eliminating a major source of ASM implicated in central neuronal autophagic dysfunction, and it decreases tight junction expression in BMECs, allowing subsequent RVG-pSL@FIN/RSV not internalized by BMECs to penetrate the brain parenchyma through intercellular spaces, thus continuing to target neuronal cells. Upon uptake by neurons, RVG-pSL@FIN/RSV releases FIN and RSV to restore autophagic function. The RVG peptide modification of this drug delivery system serves dual purposes: it initially targets BMECs, where FIN release facilitates access to the brain by promoting trans-BBB transport, and subsequently, additional drug delivery systems arriving at the BBB pass through this "door" to efficiently target neurons. This sequential mechanism accomplishes dual-targeting of both BMECs and neurons with a single drug delivery system.

2 Experimental

2.1 Materials

DOPE, phosphatidylcholine (PC), CHEMS, cholesterol (CHOL), RSV, fingolimod (FIN), 1,1'-dioctadecyl-3,3,3',3'-tetramethylindotricarbocyanine iodide (DiR), and 1,1'-dioctadecyl-3,3,3',3'-tetramethylindocarbocyanine perchlorate (DiI) were obtained from Aladdin (Shanghai, China). 1,2-Distearoyl-sn-glycero-3-phosphoethanolamine-N-(amino(polyethylene glycol)-2000] (DSPE-mPEG$_{2000}$) was obtained from Ponsure Biological (Shanghai, China), and 1,2-distearoyl-sn-glycero-3-phosphoethanolamine-polyethylene glycol 2000-rabies virus glycoprotein peptide (DSPE-PEG$_{2000}$-RVG) was obtained from GL Biochem (Shanghai) Co., Ltd. (Shanghai, China). Enzyme-linked immunosorbent assay (ELISA) plates were purchased from ExCell Bio (Shanghai, China).

2.2 Cell lines and animals

Human neuroblastoma cell line SH-SY5Y, mouse brain endothelial cell line bEnd.3 and mouse hippocampal neuronal cell line HT-22 were purchased from Cell Bank/Stem Cell Bank, Chinese Academy of Sciences (Shanghai, China). All cells were cultured in Dulbecco's modified Eagle's medium (DMEM, Gibco) containing 10% fetal bovine serum (FBS, Gibco) and 1% Penicillin/Streptomycin in a 5% CO_2 atmosphere at 37 °C.

C57BL/6 mice (10 weeks old, 19–21 g) were purchased from Hangzhou Ziyuan Laboratory Animal Technology Co., Ltd. (Hangzhou, China). All mice were provided *ad libitum* access to water and standard rodent chow, and housed under controlled environmental conditions (constant temperature (~ 25 °C), humidity (45%–60%), and 12 h dark/light cycle). All animal procedures were conducted following the guidelines of the ethical committee of Zhejiang University. The animal ethics approval number is ZJU20250786.

2.3 Preparation and characterization of RVG-pSL@FIN/RSV

To synthesize RVG-pSL@FIN/RSV, the following components were precisely weighed: 12.0 mg of DOPE, 6.0 mg of PC, 7.8 mg of CHEMS, 6.0 mg of DSPE-PEG2000-RVG, 1.0 mg of RSV, and 2.0 mg of FIN. These components were dissolved in 10 mL of dichloromethane:methanol mixture (2:1 v/v) to form a homogeneous solution. The resulting solution was transferred to a round-bottom flask and subjected to solvent evaporation using a rotary evaporator (37 °C, 100 rpm, 30 min) under reduced pressure until a uniform lipid film formed on the inner wall of the flask. Then 6 mL of phosphate-buffered saline (PBS) was added to the flask, and the lipid film was hydrated by gentle agitation or vortexing. The hydrated crude liposome suspension was transferred into a hand-extruder and subjected to sequential extrusion through a 0.2 μm polycarbonate membrane for 10 cycles to yield RVG-pSL@FIN/RSV. The extrusion process was performed manually at 25 °C with steady and consistent pressure to ensure reproducibility. Blank liposomes were prepared without adding FIN or RSV, while maintaining the same formulation and preparation conditions as the drug-loaded liposomes. For the preparation of RVG-LPs@FIN/RSV, PC was substituted for DOPE at equimolar concentrations, while CHOL replaced CHEMS at equivalent molar ratios. In the synthesis of non-RVG-modified liposomes, DSPE-mPEG2000 was utilized as a replacement for DSPE-PEG2000-RVG. Unencapsulated drug was separated by centrifugal filtration through Sephadex G-50 dextran gel columns (Beyotime). The encapsulation efficiency was calculated according to the following equation (Eq. (1)):

$$\mathrm{EE\%} = \frac{M_{\mathrm{loaded}}}{M_{\mathrm{added}}} \times 100\% \quad (1)$$

where M_{loaded} represents the mass of drug loaded in liposomes and M_{added} indicates the total amount of drug used during liposome preparation. Methanol was employed to disrupt the liposomes for determination of FIN and RSV content. Chromatographic separation was performed on a C18 reversed-phase column (Agilent, USA) maintained at 25 °C. The mobile phase consisted of acetonitrile:water (1% trifluoroacetic acid (TFA)) (55:45, v/v) at a flow rate of 1 mL/min. The detection wavelengths were 215 nm for FIN and 242 nm for RSV. After appropriate dilution with deionized water at a dilution ratio of 1:100 (v/v), the particle size, polydispersity index (PDI), and zeta potential of both liposomal formulations were measured using a ZetaSizer Nano-ZS system (Malvern, UK) at 25 °C. Each sample was equilibrated for 2 min prior to measurement, and all measurements were performed in triplicate (n = 3). The morphology of liposomes was observed using transmission electron microscopy (TEM, JEM-1230, JEOL). To evaluate the stability of liposomes, RVG-pSL@FIN/RSV was stored at 4 °C protected from light in PBS or PBS supplemented with 10% FBS, and the particle size and PDI were measured daily for a period of 7 days.

2.4 *In vitro* drug release

The *in vitro* drug release profiles of RVG-pSL@FIN/RSV and RVG-LPs@FIN/RSV were assessed by dialysis. PBS (pH 7.4 or 5.0) supplemented with 1% (v/v) Tween 80 served as the release medium. Liposome samples were transferred into dialysis bags (molecular weight cut-off (MWCO): 3.5 kDa) and immersed in 10 mL of release medium in a shaking water bath maintained at 37 °C and 100 rpm. At designated time points (0.5, 1, 2, 4, 8, 12, 24, 48, and 72 h), 2 mL aliquots of the release medium were withdrawn and replenished with an equal volume of fresh medium. Prior to analysis, collected samples (100 μL) were treated with methanol to disrupt the liposomes, and FIN and RSV concentrations were quantified by high-performance liquid chromatography (HPLC) as described in Section 2.3.

2.5 *In vitro* cytotoxicity

The MTT (methylthiazolyldiphenyl-tetrazolium bromide) assay was performed to evaluate the cytotoxicity of blank liposomes on bEnd.3, HT-22, and SH-SY5Y cells. Cells in the logarithmic growth phase were seeded into 96-well plates at a density of 8×10^3 cells per well and cultured until reaching approximately 80% confluence. The medium was then replaced with fresh medium containing blank liposomes at various concentrations, with each concentration tested in triplicate. After 24 or 48 h of incubation, 20 μL of MTT solution (5 mg/mL) was added to each well and incubated for an additional 4 h at 37 °C. The medium was subsequently aspirated, and 200 μL of dimethyl sulfoxide (DMSO) was added to each well to solubilize the formazan crystals. The plates were shaken at 300 rpm for 10 min at 37 °C, and the absorbance was measured at 570 nm using a microplate reader (Model 680; Bio-Rad, Hercules, CA, USA).

2.6 *In vitro* cellular uptake

Cellular uptake of DiI-labeled liposomes was investigated using bEnd.3 cells as an *in vitro* model. Cells were seeded in 12-well culture plates at a density of 1.0×10^5 cells per well and cultured until approximately 80% confluence was achieved. Subsequently, cells were incubated with either pSL@DiI or RVG-pSL@DiI formulations, where the final concentration of DiI was 5 μM. Following incubation periods of either 1 or 4 h, the culture medium was aspirated and cells were gently washed three times with cooled PBS to remove non-internalized liposomes. Cells were then detached using 0.25% trypsin-EDTA solution, collected by centrifugation (1000 rpm, 5 min), and resuspended in cold PBS. All samples were sieved and then measured by flow cytometry. The mean fluorescence intensity (MFI) was calculated to evaluate the cellular internalization efficiency of different liposomal formulations.

2.7 Assessment of enhanced trans-BBB transport of RVG-pSL@FIN/RSV *in vitro*

An *in vitro* BBB model was established to evaluate the BBB-opening capacity of RVG-pSL@FIN/RSV. bEnd.3 cells were seeded onto polycarbonate membrane filters (pore size: 0.4 μm, surface area: 1.12 cm^2) in Transwell inserts (Costar Transwell, Millipore Corp., Bedford, MA, USA). Transendothelial electrical resistance (TEER) was measured using a Millicell-ERS volt-ohmmeter (Millipore Co., USA). The *in vitro* BBB model was considered successfully established when TEER values exceeded 150 Ω·cm^2, indicating formation of tight junctions characteristic of a physiological barrier. Once the BBB model was established, cells were treated with either free drugs or liposomal formulations containing FIN and RSV at final concentrations of 5 μM FIN and 2 μM RSV. After 24 h incubation at 37 °C, TEER values were measured again to assess changes in barrier integrity. Following TEER measurements, culture medium was removed from both apical and basolateral

chambers and replaced with pre-warmed Hank's Balanced Salt Solution (HBSS). Fluorescein isothiocyanate (FITC)-Dextran solution (10 kDa, final concentration 0.5 mg/mL) was added to the apical chamber. After 4 h incubation, basolateral chamber solutions were collected for fluorescence analysis. Fluorescence intensity was measured by spectrofluorometry at excitation and emission wavelengths of 490 and 520 nm, respectively. FITC-Dextran concentrations in the basolateral chamber were calculated using a standard curve correlating fluorescence intensity with FITC-Dextran concentration. For the *in vitro* BBB co-culture model, bEnd.3 cells were seeded in the apical chamber as described above, while HT-22 cells were seeded on coverslips in the basolateral chamber at a density of 5×10^4 cells per well. DiI-labeled liposomes were added to the apical chamber at 0, 24, and 48 h (0.77 μg FIN and 3 μg DiI per addition). At 2 h after each addition, all basolateral medium was removed for fluorescence intensity measurement, and an equal volume of fresh medium was immediately replenished. At 50 h, DiI uptake by HT-22 cells was assessed by confocal laser scanning microscopy (CLSM).

2.8 *In vivo* biodistribution study of RVG-pSL

C57BL/6 mice were randomly divided into three groups (n = 3–4/group). Prior to administration, the hair over the cranial region was carefully removed to facilitate fluorescence imaging. Mice received a single dose of free DiR, pSL@DiR, or RVG-pSL@DiR via tail vein injection at a DiR dose of 0.3 mg/kg body weight. Brain accumulation of the formulations was monitored at predetermined time points by *in vivo* imaging system (IVIS) Spectrum. At the terminal time point, mice were deeply anesthetized and subjected to transcardial perfusion with physiological saline to eliminate blood-associated fluorescence signals. The brain and major peripheral organs were harvested. *Ex vivo* fluorescence imaging of the isolated organs was performed immediately. The mean fluorescence intensity in each organ was quantified using the system's image analysis software.

2.9 Assessment of enhanced trans-BBB transport following RVG-pSL@FIN/RSV administration

To evaluate the BBB transport-promoting effects of RVG-pSL@FIN/RSV *in vivo*, C57BL/6 mice were randomly divided into three experimental groups (n = 3–4/group): (1) RVG-pSL@FIN/RSV (FIN dose: 2.5 mg/kg), (2) positive control SC79 (5 mg/kg), and (3) physiological saline control group (equivalent volume). All formulations were administered via tail vein injection. At 24 h post-administration, mice received an intravenous injection of Evans blue solution (2 mg/mL in physiological saline) at a dose of 10 mg/kg. Following a 2 h circulation period, mice were deeply anesthetized and subjected to transcardial perfusion with physiological saline to remove intravascular dye. The brain and major peripheral organs were harvested. Tissue distribution of Evans blue was visualized by IVIS Spectrum. Quantitative analysis of dye extravasation was performed by measuring fluorescence intensity in the harvested tissues. Additionally, we evaluated the capacity of RVG-pSL@FIN/RSV to promote *in vivo* transport across the BBB in comparison with free FIN, while maintaining equivalent FIN dosages (2.5 mg/kg) and consistent experimental methodologies.

To evaluate the enhancing effect of BBB opening on the trans-BBB transport of the drug delivery system, two experimental methods were employed. In method 1, C57BL/6 mice were randomly divided into 3 groups (n = 3–4/group) and received daily tail vein injections of unlabeled RVG-LPs@FIN or RVG-pSL@FIN on days 1 and 2, with doses standardized at 2.5 mg/kg FIN. On day 3, all groups received DiR-labeled RVG-LPs (0.3 mg/kg DiR). At 2 h after the day 3 injection, brain accumulation of the formulations was monitored by IVIS Spectrum imaging. Mice were then deeply anesthetized and subjected to transcardial perfusion with physiological saline to eliminate blood-associated fluorescence signals. The brain and major peripheral organs were harvested, and *ex vivo* fluorescence imaging of the isolated organs was performed immediately. Mean fluorescence intensity in each organ was quantified using the system's image analysis software. In method 2, mice were randomly divided into 5 groups (n = 3–4/group) and received daily tail vein injections of DiR-labeled liposome formulations with different compositions for 3 consecutive days. The administered doses were standardized at 0.3 mg/kg DiR and 2.5 mg/kg FIN. At 2 h after the final administration on day 3, brain accumulation was monitored by IVIS spectrum imaging. Following the same procedures as described above, mice were perfused, organs were harvested, and *ex vivo* fluorescence imaging with quantitative analysis was performed.

2.10 Preparation of Aβ25–35 oligomers

To prepare Aβ25–35 oligomers, 1.0 mg of lyophilized Aβ25–35 peptide was dissolved in hexafluoroisopropanol (HFIP) to yield a 1 mM solution [16]. The solution was maintained at room temperature for 30 min to ensure complete monomerization of Aβ25–35 peptide. Subsequently, HFIP was eliminated via rotary evaporation. The peptide film was then reconstituted with DMSO to prepare a 5 mM stock solution. This stock was further diluted with physiological saline to a final concentration of 1 mg/mL and incubated at 37 °C for 7 days to facilitate Aβ25–35 aggregation [17]. The morphology of Aβ25–35 was observed using TEM (JEM-1230, JEOL).

2.11 Animal model

Mice were anesthetized with isoflurane via a precision vaporizer system. Following complete anesthesia, the cranial fur was removed, and animals were secured in a stereotaxic frame. A 1.0 cm midline scalp incision was made to expose the skull surface. At predetermined coordinates, a 0.8 mm diameter burr hole was drilled, with hemostasis achieved using sterile cotton swabs as needed. Stereotaxic coordinates were: anteroposterior (AP) = −2.3 mm, mediolateral (ML) = ±1.8 mm, and dorsoventral (DV) corresponding to the hippocampal target depth. Sterile Aβ25–35 solution (1 mg/mL in physiological saline, 8 μL total volume) was infused at 1.6 μL/min. Following injection, the needle was maintained in position for 2 min before gradual withdrawal. The scalp incision was closed with absorbable sutures, and bupivacaine (0.1 mg/kg) was administered subcutaneously at the incision site for post-operative analgesia. During recovery, animals were placed in clean cages on a warming platform maintained at 42 °C. Following full recovery from anesthesia, animals were returned to their home cages with *ad libitum* access to food and water.

2.12 Animal treatment

Following Aβ model establishment, AD mice were randomly allocated into two experimental cohorts: delayed treatment and immediate treatment groups. Each cohort was subdivided into four treatment arms (n = 7–8 per arm), with healthy mice serving as

controls. No significant differences in body weight were observed within or between groups. FIN-containing formulations (RVG-LPs@FIN/RSV and RVG-pSL@FIN/RSV) and free FIN were administered at 2.5 mg/kg, while RSV-containing formulations (RVG-LPs@FIN/RSV and RVG-pSL@FIN/RSV) and free RSV were administered at 1.0 mg/kg. All treatments were administered via tail vein injection once daily for 7 days, with a rest period on day 4. Control groups received equivalent volumes of physiological saline following the same schedule. The primary distinction between cohorts was treatment initiation: the delayed treatment group commenced therapy 7 days post-model establishment, whereas the immediate treatment group began 1 day post-Aβ induction.

2.13 Morris water maze study

The Morris water maze test was employed to assess the ability of RVG-pSL@FIN/RSV to ameliorate cognitive behavioral deficits in AD mice. Spatial navigation trials were conducted over 6 d. Each mouse underwent four training trials daily, with starting positions randomized across the four quadrants. Visual cues were placed on the maze walls to enable spatial navigation to the hidden submerged platform (1 cm below water surface). Each trial had a maximum duration of 60 s. If a mouse failed to locate the hidden platform within the allotted time or did not remain on the platform for 10 s, it was gently guided to the platform and allowed to remain there for 10 s to facilitate spatial memory formation. In such instances, the escape latency was recorded as 60 s. Water temperature was maintained at 22 ± 1 °C throughout all trials, and the pool was divided into four quadrants of equal size for analytical purposes. A probe trial was conducted 24 h after the final day of acquisition training to assess spatial reference memory. During this trial, the hidden platform was removed from the maze, and mice were released from the quadrant diametrically opposite to the original platform location. Each mouse was allowed to swim freely for 60 s. Swimming trajectories were tracked and recorded using a computerized video tracking system. Parameters analyzed included time spent in the target quadrant, number of platform location crossings, and swimming speed.

2.14 Western blots analysis

Following euthanasia, mouse brains were rapidly removed. A portion of the brain tissue was allocated for paraffin embedding. The remaining tissue was processed for hippocampal dissection, which was performed expeditiously. The isolated hippocampal tissues were homogenized in RIPA (radio immunoprecipitation assay) lysis buffer supplemented with protease inhibitor cocktail (1:100) and phosphatase inhibitor cocktail (1:100). The lysates were centrifuged at 14,000 rpm for 20 min at 4 °C to sediment cellular debris. Supernatants containing solubilized proteins were carefully collected, and protein concentrations were determined using the BCA assay with bovine serum albumin as the standard. A portion of each sample was allocated for dot blot analysis, while the remainder was mixed with loading buffer and heated at 100 °C for 5 min for subsequent western blot detection. For *in vitro* cellular experiments, cells were harvested by scraping from the culture surface, and the protein samples were prepared for western blot in the same way.

Equal amounts of total protein were separated by SDS-polyacrylamide gel electrophoresis and subsequently transferred to pre-activated PVDF membranes (0.22 μm, Merck Millipore, USA). Membranes were covered with block buffer for 1 h at room temperature, followed by overnight incubation with primary antibodies at 4 °C. After washing, membranes were incubated with appropriate HRP-conjugated secondary antibodies for specific protein band detection. Immunoreactive bands were visualized using enhanced chemiluminescence HRP substrate and documented with the imaging system (Bio-Rad, USA). GAPDH, β-actin, or β-tubulin served as loading controls for sample normalization. Densitometric analysis was performed using ImageJ software. The primary and secondary antibodies used in this study were as follows: anti-p62 antibody (1:10,000, Abcam), anti-LC3B antibody (1:2000, Abcam), anti-acid sphingomyelinase antibody (1:2000, HUABIO), anti-PP2A antibody (1:1000, Cell Signaling Technology), anti-BACE-1 antibody (1:1000, HUABIO), anti-p-Tau antibody (1:1000, Cell Signaling Technology), anti-β-actin antibody (1:5000, Servicebio), anti-GAPDH antibody (1:2000, Servicebio), anti-β-tubulin antibody (1:2000, Servicebio), anti-rabbit secondary antibody (1:5000, HUABIO), anti-mouse secondary antibody (1:5000, HUABIO).

2.15 Dot blot analysis

Two microliters of each protein sample were directly spotted onto a nitrocellulose membrane (0.45 μm, Bio-Rad Laboratories) and allowed to dry completely at room temperature for 30 min. After complete drying, membranes were covered with block buffer for 1 h at room temperature, followed by overnight incubation with primary antibodies at 4 °C. Following primary antibody incubation, membranes were washed with Tris-buffered saline with Tween 20 (TBST) and subsequently incubated with HRP-conjugated secondary antibodies for 1 h at room temperature. After three additional washes with TBST, immunoreactive dots were detected using enhanced chemiluminescence substrate and visualized by the imaging system (Bio-Rad, USA). Dot intensities were quantified by densitometric analysis using ImageJ software. The primary and secondary antibodies used in this study were as follows: anti-A11 antibody (1:500, Invitrogen), anti-GAPDH antibody (1:2000, Servicebio), anti-rabbit secondary antibody (1:5000, HUABIO), and anti-mouse secondary antibody (1:5000, HUABIO).

2.16 ELISA

At 24 h following the completion of treatment in the immediate treatment group, mice were deeply anesthetized and blood samples were collected via retro-orbital bleeding and immediately transferred to polypropylene tubes containing EDTA. The tubes were inverted multiple times to ensure thorough mixing with the anticoagulant. Samples were maintained on ice and promptly centrifuged at 2000×*g* the upper plasma layer was collected and stored at −80 °C. Serum amyloid A (SAA) concentrations in mouse plasma were subsequently determined using an ELISA kit.

2.17 Nissl staining

At 24 h following the completion of treatment in the immediate treatment group, mice were anaesthetized and perfused transcardially with saline and 4% paraformaldehyde. Brains were immediately removed and further fixed for 24 h to perform Nissl staining assays. Then brains were embedded in paraffin and sections of 5 μm were prepared for Nissl staining. For the delayed treatment group, identical tissue collection and histological procedures were implemented immediately following the completion of the Morris water maze study.

2.18 Immunofluorescence staining

At 24 h following the completion of treatment in the immediate treatment group, mice were anaesthetized and perfused transcardially with saline and 4% paraformaldehyde. Brains were immediately removed and further fixed for 24 h to perform immunofluorescence staining. Then brains were embedded in paraffin and sections of 5 μm. For the delayed treatment group, identical tissue collection and histological procedures were implemented immediately following the completion of the Morris water maze study. The primary and secondary antibodies used in this study were as follows: anti-acid sphingomyelinase antibody (1:2000, HUABIO), anti-GFAP antibody (1:500, Servicebio), anti-Iba1 antibody (1:500, Servicebio), FITC conjugated anti-rabbit IgG (1:200), FITC conjugated anti-mouse IgG (1:200), Cy3 conjugated anti-mouse IgG (1:200). Fluorescence micrographs were captured using an automated slide-scanning fluorescence microscope imaging system (Olympus VS200, Japan).

2.19 Hematoxylin and eosin (H&E) staining

Following the completion of the Morris water maze study, the major organs (heart, liver, spleen, lung, and kidney) of mice were removed and fixed in 4% paraformaldehyde for 24 h. Organs were embedded in paraffin and sections of 5 μm were prepared for H&E staining.

2.20 Statistical analysis

Data are presented as mean ± standard deviation (SD). Statistical significance was evaluated by Student's *t*-test and one-way ANOVA. All statistical analyses were performed using GraphPad Prism software. Representation of the *P*-value was $^{*}P < 0.05$, $^{**}P < 0.01$, $^{***}P < 0.001$.

3 Results and discussion

3.1 Characterization of RVG-pSL@FIN/RSV

The FIN-to-RSV ratio in the liposomal formulation was optimized through a series of *in vitro* cellular assays, including cytotoxicity assessments (Fig. S1 in the Electronic Supplementary Material (ESM)) and dose-response screening of free FIN and RSV (Fig. S2 in the ESM). At 1.25 μM, RSV effectively restored autophagy in Aβ25–35-treated HT22 cells (Figs. S2(a)–S2(c) in the ESM) and inhibited Aβ25–35 aggregation *in vitro* (Fig. S2(d) in the ESM). Concurrently, FIN at 5 μM downregulated claudin-5 expression in bEnd.3 cells after 24 h incubation (Figs. S2(g) and S2(h) in the ESM) and reduced transendothelial electrical resistance across the bEnd.3 monolayer (Fig. S2(i) in the ESM). Based on these optimal concentrations, RSV and FIN were co-encapsulated at a 1:4 molar ratio in liposomal formulations following removal of free drug. All liposomes in this study were prepared by thin film hydration followed by extrusion. TEM revealed that both RVG-pSL and RVG-pSL@FIN/RSV exhibited vesicular morphology with compact bilayer structures (Figs. 1(a) and 1(b)). Dynamic light scattering (DLS) analysis showed that RVG-pSL had a particle size of approximately 70.7 ± 1.6 nm (Fig. 1(c)). After loading with FIN and RSV, the particle size increased to approximately 84.7 ± 4.2 nm with a PDI of 0.16 ± 0.02 (Fig. 1(d)), and the zeta potential was −10.4 ± 3.3 mV (Fig. 1(e)). RVG-pSL@FIN/RSV achieved encapsulation efficiencies of 65.2% for RSV and 78.7% for FIN, with corresponding drug loading capacities of 1.7% and 1.8%, respectively. Within 7 days post-preparation, RVG-pSL@FIN/RSV exhibited no significant changes in particle size, PDI showed only a marginal increase, demonstrating favorable stability (Fig. 1(f)). We further measured the particle size and PDI of RVG-pSL@FIN/RSV under the same conditions in PBS supplemented with 10% FBS.

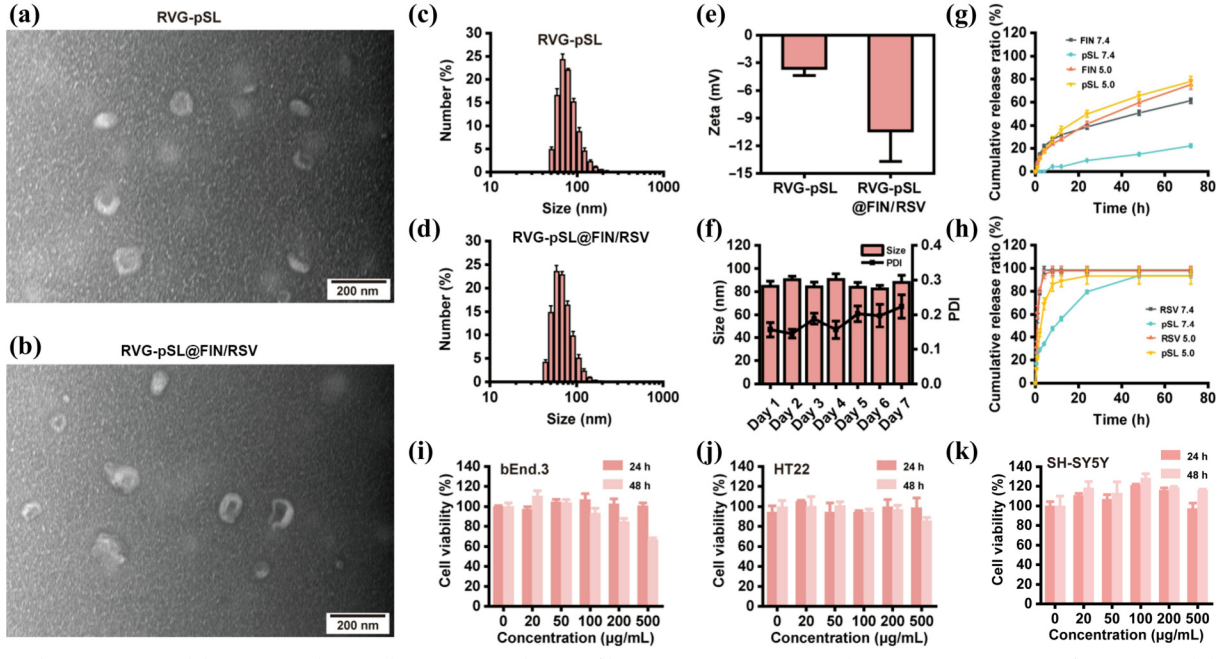

Figure 1 Characterization, stability, *in vitro* release, and cytotoxicity evaluation of liposomes. (a) Transmission electron microscopy image of RVG-pSL and (b) RVG-pSL@FIN/RSV (scale bars: 200 nm). (c) Particle size distribution of RVG-pSL and (d) RVG-pSL@FIN/RSV (n = 3). (e) Zeta potential measurements of RVG-pSL and RVG-pSL@FIN/RSV (n = 3). (f) Particle size and PDI stability of RVG-pSL@FIN/RSV over 7 days (n = 3). (g) *In vitro* cumulative release profile of FIN from RVG-pSL@FIN/RSV (n = 3). (h) *In vitro* cumulative release profile of RSV from RVG-pSL@FIN/RSV (n = 3). Cytotoxicity assessment of RVG-pSL against (i) bEnd.3 cells, (j) HT22 cells, and (k) SH-SY5Y cells (n = 3). Data are presented as mean ± SD. Statistical significance was evaluated by Student's *t*-test and one-way ANOVA.

Throughout the 7 days period, the difference between the particle size measured in PBS and that measured in PBS supplemented with 10% FBS on the corresponding day remained within 7 nm. The PDI increased from 0.16 ± 0.02 to 0.26 ± 0.01, and the day-to-day variation in PDI remained within 0.03 over 7 days (Fig. S3 in the ESM). The pH-responsive lipid components DOPE and CHEMS in the liposome formulation promote lysosomal escape. RVG-pSL@FIN/RSV exhibited accelerated release of both RSV and FIN at pH 5.0 compared to pH 7.4, confirming the pH-responsive behavior of RVG-pSL (Figs. 1(g) and 1(h)). The enhanced lysosomal escape of RVG-pSL was validated by confocal laser scanning microscopy (Fig. S4 in the ESM). DiI-labeled RVG-LPs and RVG-pSL were incubated with bEnd.3 cells, after which lysosomes were stained with LysoTracker. Colocalization analysis revealed a significantly lower colocalization coefficient between DiI and LysoTracker signals in RVG-pSL@DiI-treated bEnd.3 cells compared with the RVG-LPs@DiI group (Fig. S5 in the ESM), suggesting a reduced tendency for lysosomal localization after uptake. The results suggested that the pH-responsive formulation RVG-pSL promotes lysosomal escape compared to RVG-LPs. This lysosomal escape mechanism facilitates intracellular FIN release within bEnd.3 cells, thereby attenuating the elevated ASM activity characteristic of BMECs in AD. Moreover, FIN downregulates tight junction protein expression, transiently facilitating transport across the BBB and thereby promoting the subsequent passage of RVG-pSL into the brain. MTT assays evaluating the cytotoxicity of different concentrations of RVG-pSL on bEnd.3, HT22, and SH-SY5Y all demonstrated good safety profiles (Figs. 1(i)–1(k)).

3.2 RVG-pSL@FIN/RSV targets BMECs and reduces ASM expression

We evaluated the brain-targeting capability and ASM-reducing effects of RVG-pSL@FIN/RSV at both cellular and animal levels. Flow cytometric analysis following 1 h co-incubation of bEnd.3 cells with pSL@DiI or RVG-pSL@DiI revealed enhanced cellular uptake of RVG-modified liposomes. At 4 h, uptake of both formulations increased, with significantly greater fluorescence intensity observed for RVG-modified liposomes (Fig. 2(a)). To determine the optimal time point for assessing brain accumulation, fluorescence signals in major organs were monitored at 2 and 4 h post-intravenous administration of DiR-labeled liposomes. Tissues harvested at 2 h post-injection exhibited stronger fluorescence intensity than those at 4 h, establishing 2 h as the optimal time point for subsequent biodistribution analyses (Fig. S6 in the ESM). DiR accumulation in brain and major organs was further examined in C57BL/6 mice at 2 h following intravenous administration of free DiR, pSL@DiR, or RVG-pSL@DiR (Figs. 2(b) and 2(c)). Semi-quantitative analysis confirmed the superior brain-targeting capability of RVG-modified liposomes relative to non-modified formulations (Figs. 2(d) and 2(e)). In addition, semi-quantitative analysis of the fluorescence signals in the heart, liver, spleen, lung, and kidney at 2 h was performed (Fig. S7 in the ESM).

As previously reported, FIN reduces ASM expression across multiple cell types. To validate this effect *in vitro*, bEnd.3 cells were stimulated with tumor necrosis factor-α (TNF-α) to elevate ASM levels, followed by 24 h co-incubation with varying FIN concentrations [6]. Western blot analysis confirmed that FIN reversed inflammatory cytokine-induced ASM upregulation in bEnd.3 cells (Figs. S2(e) and S2(f) in the ESM). The ASM-reducing efficacy of RVG-pSL@FIN/RSV was subsequently evaluated *in vivo* using Aβ25–35-induced AD mouse models. The aggregation of Aβ25–35 after incubation was examined by TEM (Fig. S8 in the ESM). Mice in the delayed treatment cohort received therapeutic interventions 7 days post-Aβ25–35 injection as described in Section 2.12. The key experimental time points were indicated in the schematic timelines (Fig. S9 in the ESM). Following Morris water maze testing, hippocampal proteins were extracted for biochemical analysis. Western blot results demonstrated that RVG-pSL@FIN/RSV treatment significantly reduced hippocampal ASM expression by 29.7% compared to Aβ25–35-treated mice, approaching levels observed in healthy controls (Figs. 2(f) and 2(g)). In contrast, RVG-LPs@FIN/RSV treatment did not significantly reduce ASM levels, likely due to suboptimal FIN release kinetics from conventional liposomes lacking pH-responsive mechanisms for endosomal drug release. Immunofluorescence staining was performed to examine ASM distribution in hippocampal tissue and treatment-induced changes. Representative images of the dentate gyrus (DG) region revealed that hippocampal ASM was predominantly localized to BMECs rather than neurons (Fig. 2(h)). Compared to Aβ25–35-induced model mice, animals treated with RVG-pSL@FIN/RSV exhibited markedly reduced ASM fluorescence intensity in the hippocampal DG region (Figs. 2(i) and 2(j)). CD31 is widely accepted as a classic, foundational marker for identifying BMECs. Co-immunostaining with CD31 showed a significant reduction in CD31-colocalized ASM fluorescence in the DG region after RVG-pSL@FIN/RSV treatment, further indicating decreased ASM expression in BMECs (Fig. S10 in the ESM). Collectively, these findings demonstrate that RVG-pSL@FIN/RSV possesses effective brain-targeting capability, successfully downregulates ASM expression in BMECs of AD mice, and promotes the restoration of central neuronal autophagy through ASM reduction.

3.3 RVG-pSL@FIN/RSV promotes transport across the BBB

RVG-pSL@FIN/RSV modulates BBB transport properties, thereby facilitating liposomal passage and enhancing trans-BBB delivery efficiency. Alzheimer's disease is characterized by compromised BBB integrity and increased permeability. Upon therapeutic intervention, BBB inflammation subsides and barrier function is progressively restored, reducing paracellular leakage. Consequently, transiently and reversibly facilitating transport across the BBB to promote nanocarrier delivery represents a promising strategy for enhancing drug delivery in AD treatment.

We evaluated the ability of RVG-pSL@FIN/RSV to promote transport across the BBB at both cellular and animal levels. TEER measurements using an *in vitro* BBB model demonstrated that both free FIN and RVG-pSL@FIN reduced TEER by approximately 6 $\Omega \cdot cm^2$, regardless of RSV presence, indicating that RSV does not interfere with FIN-mediated BBB modulation. In contrast, RVG-LPs@FIN and RVG-LPs@FIN/RSV lacking lysosomal escape capability exhibited only modest TEER reduction of approximately 3 $\Omega \cdot cm^2$, confirming the critical role of lysosomal escape in facilitating effective FIN release (Fig. 3(a)). FIN exhibits pH-dependent solubility and amphiphilic properties, enabling efficient liposomal encapsulation but hindering spontaneous release. The acidic lysosomal environment, coupled with membrane fusion during pSL-mediated lysosomal escape, accelerates FIN release into the cytoplasm where it exerts its pharmacological activity. This was further corroborated by FITC-dextran transport assays (Fig. 3(b)).

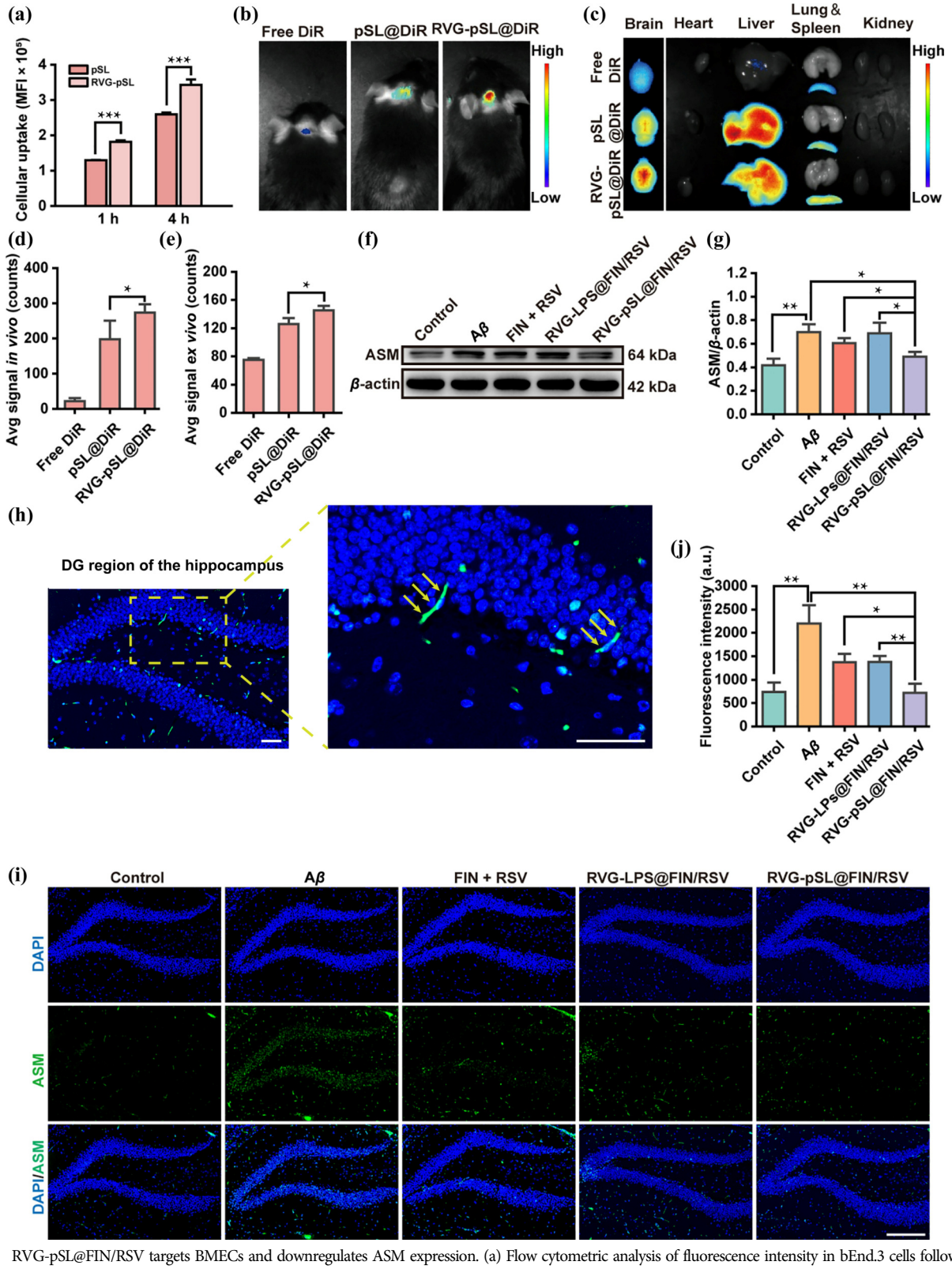

Figure 2 RVG-pSL@FIN/RSV targets BMECs and downregulates ASM expression. (a) Flow cytometric analysis of fluorescence intensity in bEnd.3 cells following co-incubation with pSL@DiI or RVG-pSL@DiI (n = 3). (b) Representative *in vivo* fluorescence images of mouse brains at 2 h post-administration of free DiR, pSL@DiR, and RVG-pSL@DiR. (c) *Ex vivo* fluorescence images of major organs harvested at 2 h post-administration of free DiR, pSL@DiR, and RVG-pSL@DiR. (d) Semi-quantitative analysis of *in vivo* brain fluorescence intensity (n = 5). (e) Semi-quantitative analysis of *ex vivo* brain fluorescence intensity (n = 3). (f) Western blot analysis of hippocampal ASM expression across experimental groups and (g) corresponding densitometric quantification (n = 3). (h) Representative immunofluorescence micrographs of ASM expression in the DG region of the hippocampus (scale bars: 50 μm). (i) Representative immunofluorescence micrographs of ASM expression in DG region at 7 days post-treatment (scale bar: 200 μm), with (j) corresponding semi-quantitative fluorescence intensity analysis (n = 3). Data are presented as mean ± SD. Statistical significance was evaluated by Student's t-test and one-way ANOVA. *P < 0.05, **P < 0.01, ***P < 0.001.

Both free FIN and RVG-pSL formulations significantly increased FITC-dextran transport into the basolateral chamber by approximately 10.0%, independent of RSV presence, confirming enhanced trans-BBB transport. To validate the trans-BBB transport capability of FIN-loaded RVG-pSL *in vitro*, a BBB co-culture model was constructed (Fig. 3(c)). The bEnd.3 monolayer simulated BMECs, while HT22 cells in the basolateral chamber represented neuronal cells. DiI-labeled liposomes were added to the apical chamber at 0, 24, and 48 h, and DiI fluorescence intensity in the basolateral medium was measured 2 h following each addition. At 50 h, DiI uptake by HT22 cells was assessed by confocal laser scanning microscopy. At a FIN concentration of 5 μM, the basolateral DiI fluorescence intensity in the RVG-pSL@FIN group at 50 h was 3.1-fold higher than that of the RVG-pSL group (Fig. 3(d)), demonstrating that FIN-mediated BBB modulation significantly enhances trans-BBB delivery. In contrast, the RVG-LPs@FIN group exhibited low BBB penetration, underscoring the critical role of lysosomal escape in facilitating FIN release. At 50 h, only HT22 cells exposed to RVG-pSL@FIN displayed substantial DiI fluorescence signals, further corroborating these findings (Figs. 3(e) and 3(f)). We subsequently evaluated the trans-BBB transport efficiency of RVG-pSL@FIN *in vivo*. Fluorescence imaging of Evans blue extravasation 24 h post-intravenous administration revealed that RVG-pSL@FIN demonstrated comparable BBB-opening efficacy to the free FIN (Figs. 3(g) and 3(h)). Then we investigated whether this BBB-opening effect enhanced CNS penetration of the delivery system. Two experimental methods were used to evaluate the self-promoting brain accumulation of RVG-pSL@FIN *in vivo*. In method 1, mice were administered unlabeled RVG-LPs@FIN or RVG-pSL@FIN via tail vein injection on days 1 and 2. On day 3, all groups received DiR-labeled RVG-LPs, and brain fluorescence signals were subsequently monitored 2 h post-injection. Method 2 consisted of daily injections of DiR-labeled liposomes with different formulations, followed by assessment of brain fluorescence signals at 2 h post-injection on day 3. Corresponding to method 1, Figs. 3(i) and 3(j) show representative fluorescence images and semi-quantitative analysis, which revealed substantially higher signal accumulation in the brains of mice pre-treated with RVG-pSL@FIN. For method 2, Figs. 3(k)–3(m) present fluorescence images and semi-quantitative data, again showing markedly enhanced brain signal accumulation in the RVG-pSL@FIN group. Together, these results demonstrated that RVG-pSL@FIN/RSV can promote transport across the blood-brain barrier and facilitate its own brain accumulation.

3.4 RVG-pSL@FIN/RSV inhibits the aggregation of pathogenic proteins

After passing through the BBB, RVG-pSL@FIN/RSV selectively targets neurons via the RVG moiety, facilitating receptor-mediated endocytosis. Upon neuronal internalization, the pH-responsive liposomal carrier releases RSV and FIN to restore autophagic pathways. The therapeutic efficacy of RSV and FIN manifests through dual mechanisms: suppressing de novo synthesis of Aβ and p-Tau while enhancing clearance of pre-existing pathological proteins, both ultimately contributing to autophagy restoration. To mechanistically delineate these distinct neuroprotective actions, we implemented an immediate intervention protocol wherein therapeutic administration coincided precisely with Aβ injection, thereby specifically evaluating the capacity of RVG-pSL@FIN/RSV to inhibit initial synthesis of Aβ and p-Tau. Following intracerebroventricular injection of Aβ25–35, at least 1 week is required to induce endogenous amyloid protein generation pathways that elevate Aβ levels and promote tau hyperphosphorylation [18]. Therefore, immediate drug intervention after Aβ injection allows specific assessment of the formulation's ability to prevent Aβ and p-Tau formation. We initiated RVG-pSL@FIN/RSV treatment concurrently with surgical Aβ injection in mice, as described in Section 2.12. The key experimental time points were indicated in the schematic timelines (Fig. S9 in the ESM). At 24 h after the final treatment, western blot analysis was performed to assess changes in hippocampal beta-site amyloid precursor protein (APP) cleaving enzyme-1 (BACE-1) and PP2A expression (Fig. 4(a)). BACE-1 catalyzes the rate-limiting step in APP cleavage, leading to generation of neurotoxic Aβ [19], while PP2A plays a crucial regulatory role in tau homeostasis by catalyzing p-Tau dephosphorylation [20]. Following RVG-pSL@FIN/RSV administration, hippocampal BACE-1 expression decreased significantly by 31.1% compared to the Aβ model group, while PP2A levels increased by 59.0% (Figs. 4(b) and 4(c)), indicating that RVG-pSL@FIN/RSV effectively suppressed Aβ and p-Tau formation in AD mice. Dot blot analysis revealed that protein aggregate content in the hippocampus was significantly reduced by 26.0% following treatment (Figs. 4(d) and 4(e)). Nissl staining was employed to assess hippocampal neuronal density (Fig. 4(g)), demonstrating that RVG-pSL@FIN/RSV administration attenuated Aβ-induced neuronal death. Immunofluorescence staining revealed that RVG-pSL@FIN/RSV treatment alleviated Aβ-triggered activation of microglia and astrocytes, thereby reducing hippocampal neuroinflammation (Fig. 4(h)). We also examined changes in SAA levels (Fig. 4(f)). In Alzheimer's disease, SAA may be produced locally in the brain, co-localizes with amyloid plaques, and contributes to inflammatory responses [21]. Following RVG-pSL@FIN/RSV treatment, serum SAA content decreased by 11.1% compared to the Aβ group. Collectively, these findings demonstrate that RVG-pSL@FIN/RSV inhibits Aβ and p-Tau formation, thereby promoting restoration of neuronal autophagy.

3.5 Reversal of spatial cognitive deficits in Aβ25–35-induced C57BL/6 mice through RVG-pSL@FIN/RSV intervention

To demonstrate that RVG-pSL@FIN/RSV can clear accumulated pathogenic proteins, restore autophagy, and ultimately reverse cognitive deficits in AD mice, we established a delayed treatment protocol wherein treatment was administered 7 days after Aβ injection (detailed methods described in Section 2.12). Morris water maze testing commenced 24 h after the final treatment. Representative swimming trajectories of mice from each group were recorded (Fig. 5(a)). Normal animals typically display a progression in search strategies with increased training, transitioning from "thigmotaxis" to "random", "scanning", and finally "direct" patterns. Normal mice adopted a direct search strategy to locate the platform after training, whereas Aβ25–35 model mice predominantly employed thigmotaxis. Following RVG-pSL@FIN/RSV intervention, mice were able to locate the platform using a scanning strategy. Compared to normal mice, Aβ25–35 model mice exhibited significantly prolonged escape latency and reduced platform crossings. Following RVG-pSL@FIN/RSV treatment, escape latency was markedly decreased while platform crossing frequency significantly increased (Figs. 5(b) and 5(c)),

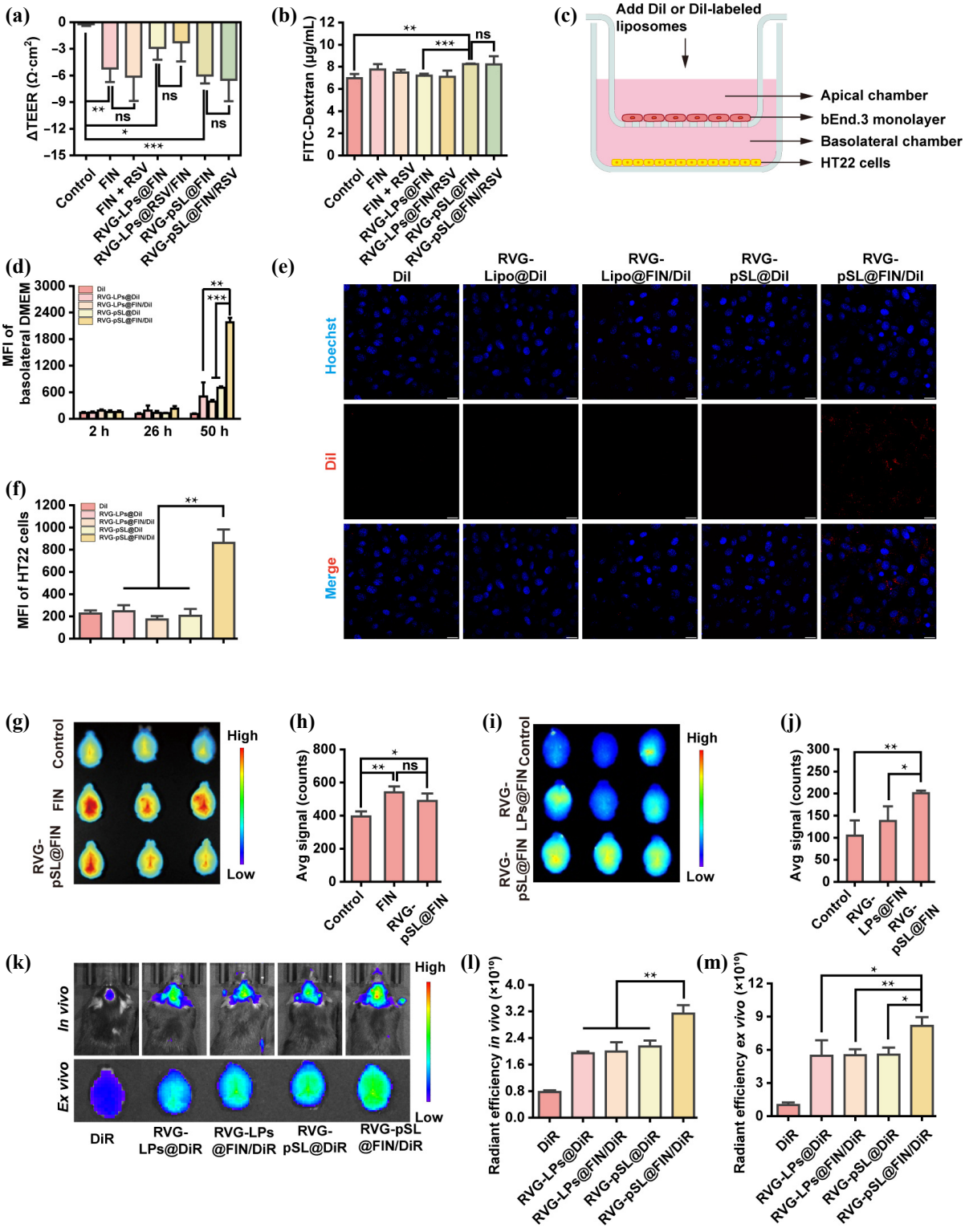

Figure 3 RVG-pSL@FIN/RSV promotes transport across the BBB. (a) TEER values following 24 h exposure of the *in vitro* BBB model to FIN and FIN-loaded liposomes, and (b) corresponding FITC-dextran transport across the BBB model ($n = 3$). (c) Schematic illustration of the *in vitro* BBB co-culture model. DiI or DiI-labeled liposomes were added to the apical chamber at 0, 24, and 48 h, and DiI MFI in the basolateral chamber medium was measured at 2, 26, and 50 h. At 50 h, DiI uptake by HT22 cells in the basolateral chamber was assessed by confocal laser scanning microscopy. (d) DiI MFI in basolateral chamber medium at 2, 26, and 50 h ($n = 3$). (e) Confocal laser scanning microscopy images of DiI fluorescence in HT22 cells in the basolateral chamber at 50 h (scale bar: 20 μm), with (f) corresponding quantification ($n = 3$). (g) Representative fluorescence images of Evans blue extravasation in mouse brains at 24 h post-administration of RVG-pSL@FIN or free FIN, with (h) corresponding quantification ($n = 3$). (i) *Ex vivo* fluorescence imaging of brain tissue from mice receiving 2 days of intravenous administration of different liposomal formulations followed by DiR-labeled liposome injection on day 3, with (j) corresponding quantification ($n = 3$). (k) Fluorescence imaging of mouse brains at day 3 post-administration of DiR-labeled liposomes, with corresponding quantification of radiant efficiency of (l) *in vivo* and (m) *ex vivo* ($n = 3$). Data are presented as mean ± SD. Statistical significance was evaluated by Student's *t*-test and one-way ANOVA. $^{*}P < 0.05$, $^{**}P < 0.01$, $^{***}P < 0.001$.

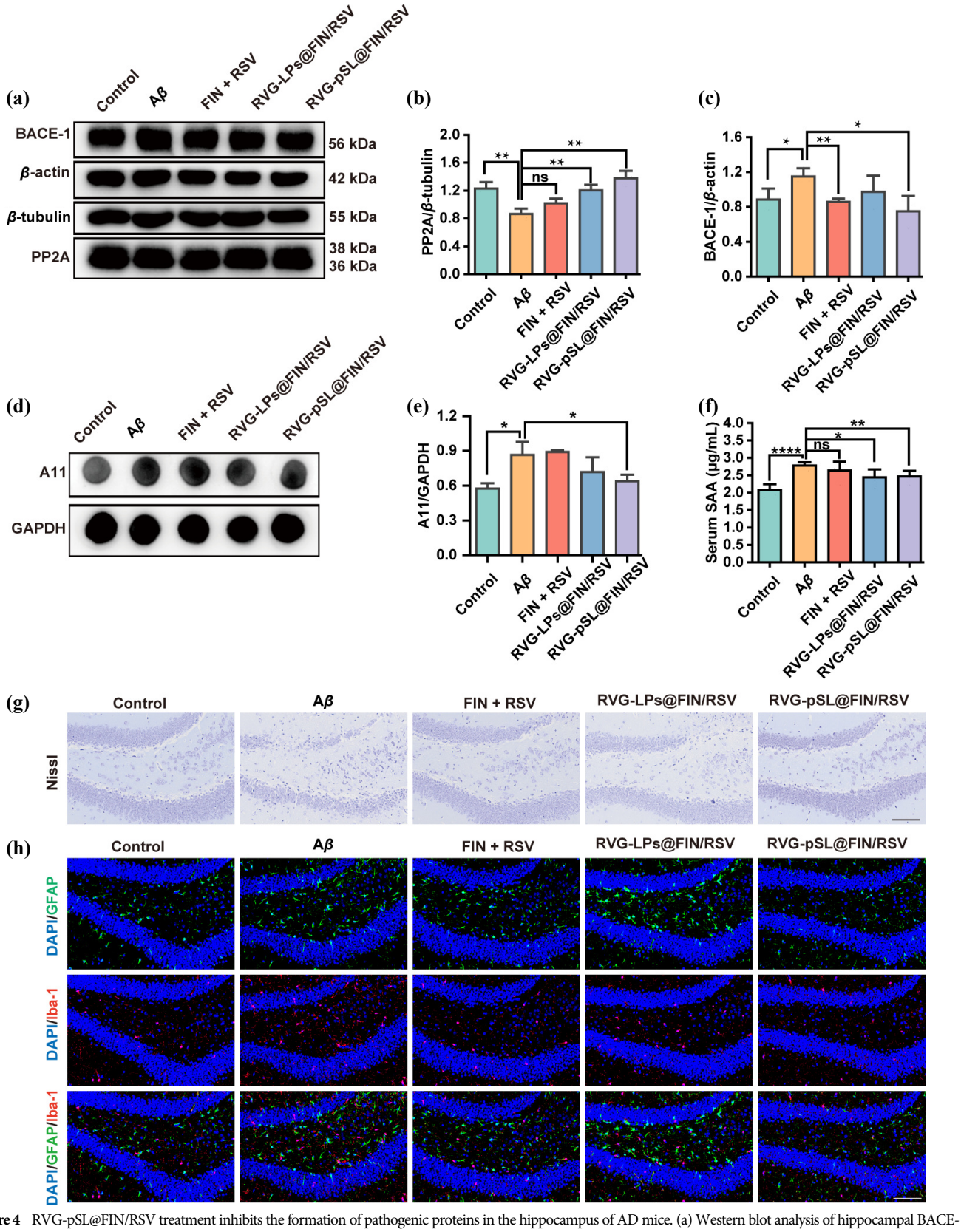

Figure 4 RVG-pSL@FIN/RSV treatment inhibits the formation of pathogenic proteins in the hippocampus of AD mice. (a) Western blot analysis of hippocampal BACE-1 (involved in Aβ formation) and PP2A (involved in p-Tau clearance) expression in different treatment groups, with corresponding semi-quantitative analysis of (b) PP2A and (c) BACE-1 (n = 3). (d) Dot blot analysis of protein aggregate content in mouse hippocampus with (e) semi-quantitative analysis (n = 3). (f) SAA levels measured by ELISA in different treatment groups (n = 5). (g) Representative images of Nissl-stained hippocampal sections from different treatment groups (scale bar: 200 μm). (h) Immunofluorescence staining for inflammatory factors in hippocampal sections across treatment groups (scale bar: 200 μm). Data are presented as mean ± SD. Statistical significance was evaluated by Student's t-test and one-way ANOVA. *P < 0.05, **P < 0.01, ***P < 0.001, ****P < 0.0001.

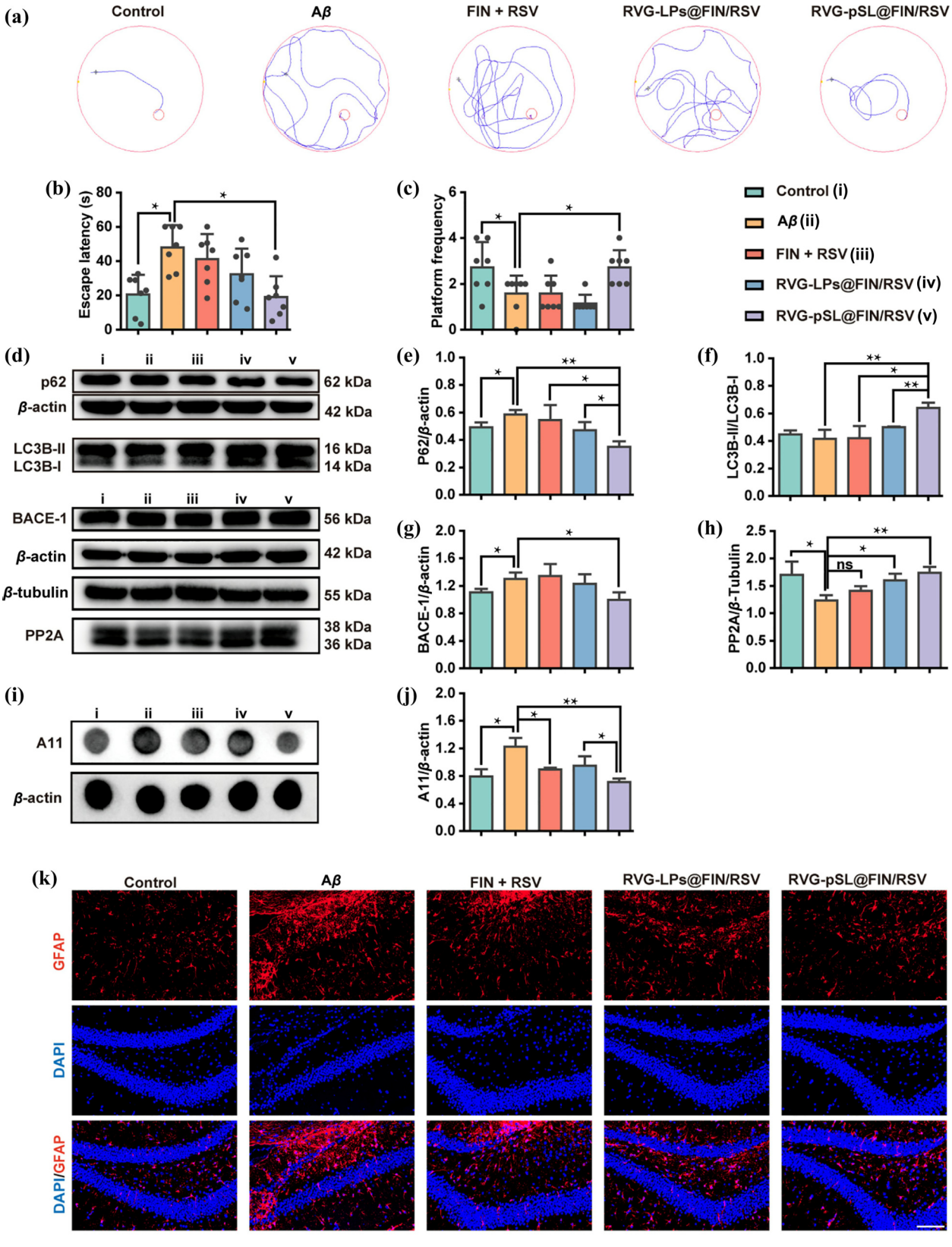

Figure 5 RVG-pSL@FIN/RSV treatment reverses cognitive deficits and alleviates neuronal autophagy dysfunction in AD mice. (a) Representative swimming trajectories of mice from each group during the Morris water maze test. (b) Escape latency and (c) number of platform crossings for each group (n = 7). (d) Western blot analysis of hippocampal autophagy-related proteins (p62, LC3B), BACE-1 (involved in Aβ formation), and PP2A (involved in p-Tau clearance) with (e)–(h) corresponding semi-quantitative analysis (n = 3). (i) Dot blot analysis of protein aggregate content in mouse hippocampi with (j) corresponding semi-quantitative analysis (n = 3). (k) Immunofluorescence staining for inflammatory factors in hippocampal sections across treatment groups (scale bar: 200 μm). Data are presented as mean ± SD. Statistical significance was evaluated by Student's t-test and one-way ANOVA. *P < 0.05, **P < 0.01.

indicating that RVG-pSL@FIN/RSV treatment reversed cognitive deficits in AD mice.

We subsequently examined changes in hippocampal protein expression by western blot (Fig. 5(d)). p62 (SQSTM1) functions as a selective autophagy receptor that binds ubiquitinated substrates and interacts with LC3B on autophagosomal membranes, facilitating cargo recruitment to autophagosomes. The conversion of LC3B-I to LC3B-II and degradation of p62 serve as critical indicators of autophagic flux [22]. Following RVG-pSL@FIN/RSV intervention, hippocampal p62 levels were significantly reduced by 40.2% compared to the Aβ model group, and the LC3B-II/LC3B-I ratio was significantly elevated by 34.9%, suggesting that RVG-pSL@FIN/RSV treatment reversed Aβ-induced autophagy impairment (Figs. 5(e) and 5(f)). These *in vivo* findings are consistent with our cellular-level observations (Fig. S11 in the ESM). We further investigated BACE-1 (involved in Aβ formation) and PP2A (involved in p-Tau dephosphorylation). Compared to the Aβ model group, RVG-pSL@FIN/RSV treatment reduced BACE-1 expression by 23.3% and increased PP2A expression by 40.9%, indicating decreased hippocampal Aβ and p-Tau formation (Figs. 5(g) and 5(h)). Dot blot analysis using A11 antibody, which recognizes protein aggregates, revealed a 41.8% reduction in hippocampal protein aggregate content following RVG-pSL@FIN/RSV treatment (Figs. 5(i) and 5(j)). Nissl staining was employed to assess hippocampal neuronal density. Following Aβ modeling, substantial neuronal loss was observed in the hippocampal DG region, while RVG-pSL@FIN/RSV treatment significantly increased neuronal numbers compared to the model group (Fig. S12 in the ESM). Immunofluorescence staining revealed that RVG-pSL@FIN/RSV reversed the extensive Aβ-induced astrocyte activation in the hippocampal DG region, suggesting alleviation of neuroinflammation (Fig. 5(k)).

To assess the safety profile of the formulation, H&E staining was performed on major organs. The RVG-pSL@FIN/RSV-treated group exhibited no notable histopathological abnormalities in vital organs, providing initial validation of the formulation's *in vivo* biocompatibility and safety (Fig. S13 in the ESM).

Collectively, RVG-pSL@FIN/RSV effectively cleared pathogenic proteins, reduced hippocampal neuronal autophagy, restored neuronal autophagy, and reversed cognitive deficits in AD mice.

4 Conclusions

This study elucidates the unexplored therapeutic potential of nanotechnology in reducing ASM levels in BMECs for treating Alzheimer's disease. Importantly, our findings indicate that reducing ASM secreted by BMECs plays a crucial role in restoring neuronal autophagic dysfunction in Alzheimer's disease pathology. Compared to conventional liposomes, our formulation RVG-pSL@FIN/RSV demonstrated superior efficacy in delivering FIN to BMECs, thereby reducing BMEC-derived ASM secretion by 29.7%. Additionally, RVG-pSL@FIN/RSV helps to open the BBB, improve neuronal targeting efficiency, clear neuronal Aβ and p-Tau and inhibit the formation of Aβ and p-Tau. In the Morris water maze test, AD model animals treated with RVG-pSL@FIN/RSV exhibited a 72.6% increase in platform crossing frequency and a 60.6% reduction in escape latency compared to untreated AD models. These findings demonstrate that RVG-pSL@FIN/RSV significantly alleviates neuronal autophagy dysfunction and reverses cognitive deficits, offering a promising new therapeutic strategy for Alzheimer's disease.

Electronic Supplementary Material: Supplementary material (including the *in vitro* effects of free FIN and RSV, co-localization analysis of liposomes and lysosomes, co-localization analysis of ASM and BMECs, and safety evaluation of liposomes) is available in the online version of this article at https://doi.org/10.26599/NR.2026.94908783.

Data availability

All data needed to support the conclusions in the paper are presented in the manuscript and the Electronic Supplementary Material. Additional data related to this paper may be requested from the corresponding author upon request.

Acknowledgements

The authors gratefully acknowledge the National Natural Science Foundation of China (No. 82473857).

Declaration of competing interest

All the contributing authors report no conflict of interests in this work.

Author contribution statement

Y. C. X.: Data curation, formal analysis, investigation, writing – original draft. S. Y. Y.: Investigation. Y. W.: Investigation. J. K.: Investigation. Y. L. H.: Investigation. K. W.: Investigation. G. T. S.: Investigation. Z. X. W.: Investigation. S. C.: Investigation. Y. R. Y.: Investigation. H. Y.: Supervision. F. Q. H.: Conceptualization, funding acquisition, project administration, supervision.

Informed consent

Not applicable.

Ethics statement

All animal procedures were conducted following the guidelines of the ethical committee of Zhejiang University. The animal ethics approval number is ZJU20250786.

Use of AI statement

None.

References

[1] Chu, J. J.; Zhang, W. C.; Liu, Y.; Gong, B. F.; Ji, W. B.; Yin, T.; Gao, C.; Liangwen, D. Q.; Hao, M. Q.; Chen, C. M. et al. Biomaterials-based anti-inflammatory treatment strategies for Alzheimer's disease. *Neural Regen. Res.* **2024**, *19*, 100–115.

[2] Sharma, H.; Chang, K. A.; Hulme, J.; An, S. S. A. Mammalian models in Alzheimer's research: An update. *Cells* **2023**, *12*, 2459.

[3] Bloom, G. S. Amyloid-β and tau: The trigger and bullet in Alzheimer disease. *JAMA Neurol.* **2014**, *71*, 505–508.

[4] Park, M. H.; Lee, J. Y.; Park, K. H.; Jung, I. K.; Kim, K. T.; Lee, Y. S.; Ryu, H. H.; Jeong, Y.; Kang, M.; Schwaninger, M. et al. Vascular and neurogenic rejuvenation in aging mice by modulation of ASM. *Neuron* **2018**, *100*, 167–182.e9.

[5] Choi, B. J.; Park, M. H.; Jin, H. K.; Bae, J. S. Acid sphingomyelinase as a pathological and therapeutic target in neurological disorders: Focus on Alzheimer's disease. *Exp. Mol. Med.* **2024**, *56*, 301–310.

[6] van Doorn, R.; Nijland, P. G.; Dekker, N.; Witte, M. E.; Lopes-Pinheiro, M. A.; van Het Hof, B.; Kooij, G.; Reijerkerk, A.; Dijkstra, C.; van van der Valk, P. et al. Fingolimod attenuates ceramide-induced blood-brain barrier dysfunction in multiple sclerosis by targeting reactive astrocytes. *Acta Neuropathol.* **2012**, *124*, 397–410.

[7] Dawson, G.; Qin, J. D. Gilenya (FTY720) inhibits acid sphingomyelinase by a mechanism similar to tricyclic antidepressants. *Biochem. Biophys. Res. Commun.* **2011**, *404*, 321–323.

[8] Patel, S. H.; Bachmann, M.; Kadow, S.; Wilson, G. C.; Abdel-Salam, M. M. L.; Xu, K.; Keitsch, S.; Soddemann, M.; Wilker, B.; Becker, K. A. et al. Simultaneous targeting of mitochondrial Kv1.3 and lysosomal acid sphingomyelinase amplifies killing of pancreatic ductal adenocarcinoma cells *in vitro* and *in vivo*. *J. Mol. Med.* **2023**, *101*, 295–310.

[9] Fagan, S. G.; Bechet, S.; Dev, K. K. Fingolimod rescues memory and improves pathological hallmarks in the 3xTg-AD model of Alzheimer's disease. *Mol. Neurobiol.* **2022**, *59*, 1882–1895.

[10] Jung, Y.; Lopez-Benitez, J.; Tognoni, C. M.; Carreras, I.; Dedeoglu, A. Dysregulation of sphingosine-1-phosphate (S1P) and S1P receptor 1 signaling in the 5xFAD mouse model of Alzheimer's disease. *Brain Res.* **2023**, *1799*, 148171.

[11] Wei, H.; Zhang, H. L.; Xie, J. Z.; Meng, D. L.; Wang, X. C.; Ke, D.; Zeng, J.; Liu, R. Protein phosphatase 2A as a drug target in the treatment of cancer and Alzheimer's disease. *Curr. Med. Sci.* **2020**, *40*, 1–8.

[12] Liu, L.; Dai, W. Z.; Zhu, X. C.; Ma, T. A review of autophagy mechanism of statins in the potential therapy of Alzheimer's disease. *J. Integr. Neurosci.* **2022**, *21*, 046.

[13] Sierra, S.; Ramos, M. C.; Molina, P.; Esteo, C.; Vázquez, J. A.; Burgos, J. S. Statins as neuroprotectants: A comparative *in vitro* study of lipophilicity, blood-brain-barrier penetration, lowering of brain cholesterol, and decrease of neuron cell death. *J. Alzheimers Dis.* **2011**, *23*, 307–318.

[14] Husain, I.; Akhtar, M.; Abdin, M. Z.; Islamuddin, M.; Shaharyar, M.; Najmi, A. K. Rosuvastatin ameliorates cognitive impairment in rats fed with high-salt and cholesterol diet via inhibiting acetylcholinesterase activity and amyloid beta peptide aggregation. *Hum. Exp. Toxicol.* **2018**, *37*, 399–411.

[15] Schultz, B. G.; Patten, D. K.; Berlau, D. J. The role of statins in both cognitive impairment and protection against dementia: A tale of two mechanisms. *Transl. Neurodegener.* **2018**, *7*, 5.

[16] Henríquez, G.; Mendez, L.; Varela-Ramirez, A.; Guerrero, E.; Narayan, M. Neuroprotective effect of Brazilin on amyloid β (25–35)-induced pathology in a human neuroblastoma model. *ACS Omega* **2020**, *5*, 13785–13792.

[17] Chang, W. G.; Teng, J. F. *β*-asarone prevents Aβ25-35-induced inflammatory responses and autophagy in SH-SY5Y cells: Down expression beclin-1, LC3B and up expression Bcl-2. *Int. J. Clin. Exp. Med.* **2015**, *8*, 20658–20663.

[18] Canet, G.; Zussy, C.; Hernandez, C.; Maurice, T.; Desrumaux, C.; Givalois, L. The pathomimetic oAβ_{25-35} model of Alzheimer's disease: Potential for screening of new therapeutic agents. *Pharmacol. Ther.* **2023**, *245*, 108398.

[19] Moussa-Pacha, N. M.; Abdin, S. M.; Omar, H. A.; Alniss, H.; Al-Tel, T. H. BACE1 inhibitors: Current status and future directions in treating Alzheimer's disease. *Med. Res. Rev.* **2020**, *40*, 339–384.

[20] Basheer, N.; Smolek, T.; Hassan, I.; Liu, F.; Iqbal, K.; Zilka, N.; Novak, P. Does modulation of tau hyperphosphorylation represent a reasonable therapeutic strategy for Alzheimer's disease. *From preclinical studies to the clinical trials. Mol. Psychiatry* **2023**, *28*, 2197–2214.

[21] Kindy, M. S.; Yu, J.; Guo, J. T.; Zhu, H. Apolipoprotein serum amyloid A in Alzheimer's disease. *J. Alzheimers Dis.* **1999**, *1*, 155–167.

[22] Larsen, K. B.; Lamark, T.; Øvervatn, A.; Harneshaug, I.; Johansen, T.; Bjørkøy, G. A reporter cell system to monitor autophagy based on p62/SQSTM1. *Autophagy* **2010**, *6*, 784–793.

This is an open access article under the terms of the Creative Commons Attribution 4.0 International License (CC BY 4.0, https://creativecommons.org/licenses/by/4.0/).

© The Author(s) 2026. Published by Tsinghua University Press.